

# Searching for Galactic Red Supergiants with Gaia RVS Spectra

Zehao Zhang (张泽浩)<sup>1,2</sup> , Biwei Jiang (姜碧为)<sup>1,2</sup> , Yi Ren (任逸)<sup>3</sup> , He Zhao (赵赫)<sup>4</sup> , and Ming Yang (杨明)<sup>5</sup> 

<sup>1</sup> Institute for Frontiers in Astronomy and Astrophysics, Beijing Normal University, Beijing 102206, People's Republic of China  
e-mail: [bjjiang@bnu.edu.cn](mailto:bjjiang@bnu.edu.cn)

<sup>2</sup> School of Physics and Astronomy, Beijing Normal University, Beijing 100875, People's Republic of China

<sup>3</sup> College of Physics and Electronic Engineering, Qilu Normal University, Jinan 250200, People's Republic of China

<sup>4</sup> Purple Mountain Observatory and Key Laboratory of Radio Astronomy, Chinese Academy of Sciences, 10 Yuanhua Road, Nanjing 210033, People's Republic of China

<sup>5</sup> Key Laboratory of Space Astronomy and Technology, National Astronomical Observatories, Chinese Academy of Sciences, Beijing 100101, People's Republic of China

Received xx / Accepted xx

## ABSTRACT

Red supergiants (RSGs) are essential to understanding the evolution and the contribution to the interstellar medium of massive stars. However, the number of identified RSGs within the Milky Way is still limited mainly due to the difficulty of measuring stellar extinction and distance. The release of approximately one million RVS spectra in Gaia DR3 presents new opportunity for identifying Galactic RSGs, because the equivalent width of the calcium triplet lines (EW(CaT)) in the spectra is an excellent indicator of stellar surface gravity. This work uses the RVS spectra with signal-to-noise ratio (SNR) greater than 100 to search for the Galactic RSGs. The dwarf stars and red giants are removed and the RSG candidates are selected by the location in the EW(CaT) vs.  $BP - RP$  diagram. The early-type RSG candidates (K0-M2) are then identified by  $BP - RP > 1.584$  and  $EW(\text{CaT}) > 1.1$  nm. To identify late-type RSG candidates (after M2), the criteria of the average equivalent widths of TiO in the XP spectra ( $EW(\text{TiO}) > 10$  nm, the color index  $K - W3 < 0.5$  and the period-amplitude sequence from Gaia DR3 LPV catalog are further applied to reduce the contamination of late-type red giants and asymptotic giant branch stars. This method yields 30 early-type (K0-M2) and 6196 late-type (after M2) RSG candidates, which is a significant increase to the present Galactic RSG sample. The application of this approach to the spectra with  $SNR > 50$  results in 48 early-type and 11,491 late-type RSG candidates. This preliminary analysis paves the way for more extensive research with Gaia DR4 when larger spectral datasets are expected to significantly enhance our understanding of Galactic RSG populations.

**Key words.** stars: massive – stars: late-type – stars: supergiants

## 1. Introduction

Red supergiants (RSGs) are among the most massive and luminous stars in the Universe, representing a crucial evolutionary phase for stars with initial mass between approximately 8 and 40  $M_{\odot}$  (Humphreys & Davidson 1979; Massey & Olsen 2003). RSGs are characterized by their immense size, cool temperature, complex light variability (Kiss et al. 2006; Yang & Jiang 2012; Ren et al. 2019; Ren & Jiang 2020; Zhang et al. 2024), and significant mass-loss rate (Humphreys et al. 2020; Beasor et al. 2020; Wang et al. 2021; Yang et al. 2023; Wen et al. 2024; Decin et al. 2024), which have profound affects for their subsequent evolution and eventual fate as supernovae.

Identifying RSGs in nearby galaxies has recently made great progress with the fast development of observation and new method. In the Small and Large Magellanic Clouds (SMC and LMC), the parallax, proper motions and radial velocity (RV) measured by Gaia are highly reliable parameters to select the member stars (Yang et al. 2019; Ren et al. 2021b). Though the Gaia astrometric parameters are accurate to select member stars, they are unavailable to most stars in the galaxies more distant than the SMC and LMC because of the limited sensitivity of Gaia. Instead, the color-color diagram (CCD) method is invented to select member stars. The very early attempt is carried out by

Massey (1998). They use the  $B - V/V - R$  diagram to separate the foreground dwarf stars from the member giant stars in that the  $B$  band covers some metallic lines sensitive to surface gravity. Ren et al. (2021a) improve this method by shifting the waveband to the near-infrared (NIR)  $J - H/H - K$  diagram. The NIR CCD has the advantages of being consistent with the peak of the RSG spectral energy distribution (SED) and much less affected by interstellar extinction. After the foreground stars are removed, RSGs in an external galaxy can be easily identified by their high luminosity and red color in the color-magnitude diagram (CMD) since all the member stars are at almost the same distance. Consequently, 5498 and 3055 RSGs are identified in the M31 and M33 (Ren et al. 2021a), 4823 and 2138 RSGs are identified in the LMC and SMC, and a total of 2190 RSGs are found in other 10 dwarf galaxies (Ren et al. 2021b).

The identification of RSGs in the Galaxy lags behind. The Galactic RSGs distribute at various direction and distance so that no identical proper motion, parallax or RV can be used. Thus, the astrophysical parameters like luminosity and color index should be determined to find the RSGs. However, the inhomogeneous and heavy extinction leads to the measurement of both luminosity and intrinsic color index difficult (e.g. Schödel et al. (2010)) because RSGs are located in the Galactic plane. Besides, the distance should be measured individually, while the perturbation of

the photocenter of RSGs brings about additional uncertainty in the Gaia parallax (Chiavassa et al. 2011). Instead of photometry, the identification of RSGs in the Galaxy relies heavily on spectroscopy. Indeed, the very early identification of RSGs in nearby galaxies also uses the spectral features and the RV derived from spectrum (see e.g. Humphreys et al. (1988)).

Spectrum contains abundant information for stellar classification. In particular, the near-infrared spectra are suitable for late-type stars (Kirkpatrick et al. 1991; Ginestet et al. 1994; Carquillat et al. 1997). Based on the spectral classifications by Humphreys (1978) and Garmany & Stencel (1992), Levesque et al. (2005) built a catalog of 74 Galactic RSGs, with their spectral types and effective temperature scales. Additionally, attention has been directed towards star clusters within the Milky Way, as RSGs are often found within OB associations. There are three massive RSGs-rich clusters named RSGC1, RSGC2, and RSGC3 located in a small region of the Galactic plane between  $l = 24^\circ$  and  $l = 29^\circ$  (Figer et al. 2006; Davies et al. 2007, 2008; Clark et al. 2009; Alexander et al. 2009), as well as several smaller clusters close to them (Negueruela et al. 2010, 2011, 2012). In some recent studies, Dorda et al. (2016) used principal component analysis (PCA) and support vector machine (SVM) techniques to analyze the spectral features in the calcium triplet (CaT) region, establishing the criteria to distinguish supergiants from non-supergiants. Subsequently, they applied this method to identify 197 cool supergiants in the Perseus arm (Dorda et al. 2018). Messineo & Brown (2019) selected Galactic K-M type Class I stars and identified 889 RSG candidates, by considering the Gaia DR2 astrometric data, but only a small fraction of them are confirmed as true RSGs. Furthermore, Messineo (2023) identified 20 new RSGs through an analysis of Gaia DR3 GSP-Phot and GSP-Spec parameters in combination with BP/RP spectra. More recently, Healy et al. (2024) compiled a catalog of 578 highly probable and 62 likely RSGs. Despite the Milky Way being estimated to host at least 5000 RSGs (Gehrz 1989), the currently known sample is far smaller. This discrepancy is mainly due to the limitations of spectroscopic surveys, which typically detect only the bright sources, leading to the miss of faint sources. Spectroscopy is also generally less efficient than photometry. Fortunately, Gaia DR3 includes a vast number of medium-resolution RVS spectra (Sartoretti et al. 2018, 2023; Recio-Blanco et al. 2023). Besides, the space observation avoids the absorption lines of the atmosphere, which improves the accuracy of line measurements. It offers an unprecedented opportunity to revisit the population of Galactic RSGs from a new perspective.

This work aims to create a large catalog of Galactic RSGs through a comprehensive analysis of the RVS spectra. The paper is organized as follows: Section 2 introduces the RVS spectra and the process of re-normalization, as well as the selection of the initial sample. Section 3 describes the CaT characteristics of preliminary RSG samples, followed by the selection processes of early-type and late-type RSG candidates. We discuss the known Galactic RSGs, completeness and pureness in our sample, and present an outlook for Gaia DR4 in Section 4. A summary is presented in Section 5.

## 2. Data

### 2.1. RVS spectra

Launched by the European Space Agency in 2013, the Gaia mission aims to create the most detailed three-dimensional map of our galaxy. Gaia's suite of instruments includes a highly pre-

cise astrometric detector, photometric facility, and the Radial Velocity Spectrometer (RVS, Gaia Collaboration et al. (2016)). The RVS is designed to obtain medium-resolution spectra in the wavelength range of 845-872 nm (Sartoretti et al. 2018), also known as CaT region, which is suitable to determine the RV over a wide range of metallicity. This spectral region is very valuable for studying cool stars like RSGs, as it contains strong absorption lines that are sensitive to temperature, surface gravity, and metallicity (Contursi et al. 2021; Creevey et al. 2023; Fouesneau et al. 2023), in particular, CaT itself is an excellent indicator of surface gravity (Diaz et al. 1989; Mallik 1994, 1997; Cenarro et al. 2001a,b).

Gaia DR3 includes 999,645 RVS spectra with a resolution of  $R \sim 11150$ . These spectra are wavelength-calibrated under vacuum conditions, and the majority has a signal-to-noise ratio (SNR) between 20 and 40 (Gaia Collaboration et al. 2023b). They are primarily used for measuring stellar RV (Katz et al. 2023) or for deriving GSP-Spec parameters with the Apsis pipeline (Creevey et al. 2023; Fouesneau et al. 2023; Recio-Blanco et al. 2023). The RVS spectra cover the features for a wide range of stellar types, with early-type stars being dominated by hydrogen Paschen lines, while late-type stars exhibit more metallic and molecular lines (see Figure 6 of Fouesneau et al. (2023)). The publicly released RVS spectra are normalized either by using their pseudo-continuum or by scaling with a constant (the latter for cool stars or spectra with low SNR, Gaia Collaboration et al. (2023b)). For the majority of stars, the normalized flux is set to 1. However, due to the presence of TiO band in the spectra of late-type stars which erode the pseudo-continuum, the normalization process is often incorrect for M-type stars. As a result, their spectra exhibit a pronounced slope across the entire wavelength range (e.g., Figure 17 in Cropper et al. (2018)). Given that Galactic RSGs are mostly of M-type (see Figure 5 of Levesque & Massey (2012)), it is necessary to re-normalize the spectra.

The steps for continuum re-normalization are as follows. First, the spectral regions with no apparent absorption bands are selected, indicated by red points in Figure 1, ignoring the narrow atomic lines listed in Dorda et al. (2016). Then, a linear fitting is performed to these points, and the original spectrum is divided by this fitting line to get the re-normalized spectrum. At last, the continuum of the spectrum is defined as the Gaussian mean of the points used for the linear fitting to correct for possible systematic offset. Figure 1 shows an example of this process, with the CaT measurement region marked in green. For consistency, the re-normalization is applied to all spectra, and the spectra of late-type stars are effectively flattened, while no significant difference is observed in the spectra of other-type stars before and after the correction.

### 2.2. Selection of the initial sample of Galactic stars

#### 2.2.1. Data pre-processing

To ensure that the analyzed spectra are from Galactic stars, the following criteria are applied:

1. A stellar probability greater than 99% (`classprob_dsc_combmod_star` > 0.99);
2. Stars not located in the LMC, i.e. the stars within the region  $64^\circ < \text{R.A.} < 98^\circ$ ,  $-78^\circ < \text{Decl.} < -59^\circ$  and RV greater than 100 km/s, are excluded;
3. Stars not located in the SMC, i.e. the stars within the region  $2^\circ < \text{R.A.} < 26^\circ$ ,  $-76^\circ < \text{Decl.} < -69^\circ$  and RV greater than 100 km/s, are excluded;

As a result, 7407 spectra are excluded. From the remaining spectra, only those with a SNR greater than 100 ( $\text{rvs\_spec\_sig\_to\_noise} > 100$ ) are chosen. This is done to ensure that the subsequent analysis is performed on high-quality spectra, minimizing the impact of noise on the equivalent width measurements. In the end, 118,048 spectra are retained for further analysis.

### 2.2.2. Removal of early-type stars

Because the Paschen series lines P13, P15, and P16 in early-type stars appear at similar wavelengths as the CaT (see Figure 2), the measurement of the EW(CaT) may be actually conducted to the hydrogen lines. Thus it is necessary to remove the early-type stars.

Since no strong absorption lines in the spectra of late-type stars appear near P14 (see Figure 2), the equivalent width of P14 region (EW(P14)) is used as the diagnosis of early-type stars. EW(P14) is calculated by using the `equivalent_width` function from the `specutils` package (Astropy-Specutils Development Team 2019). The continuum is determined by using the Gaussian mean of the points for the linear fitting described in Section 2.1, which is shown by the black dashed line in Figure 2 where the continuum level is 1.013 in this case. The wavelength range is set between 859-861 nm, i.e. the shaded gray region in Figure 2.

In addition to the EW(P14), the slope of the original Gaia RVS continuum derived from the linear fitting in Section 2.1 is supplemented to assure the identification of early-type stars. Because the continuum of early-type stars are not affected by broad molecular bands, the slope should be small. As shown in Figure 3, stars with significant EW(P14) indeed exhibit a small continuum slope, which supports this criterion. Specifically, stars with EW(P14) greater than 0.1 nm and a slope less than 0.0025 are classified as early-type. Consequently, a total of 12,396 stars are excluded, which are located in the black dashed box in Figure 3. Among the initial 118,048 stars in the sample, 8,157 have available `teff_esphs` values, indicating temperatures above 7,500 K, and are thus considered hot stars (Creevey et al. 2023). Notably, of the 12,396 early-type stars excluded, 8,133 (~99.7%) fall within this group, further validating the effectiveness of the early-type star identification and exclusion process.

## 3. The Galactic RSGs candidates

The RSG candidates are basically selected by the EW(CaT) in that it is generally larger for supergiants than dwarfs or giants. However, the Galactic RSGs are mostly M-type (Levesque & Massey 2012), leading to the decrease of EW(CaT) to be comparable to that of giants or even dwarfs (Jennings & Levesque 2016). Thus other parameters including the color index  $BP - RP$  and  $K - W3$  and the equivalent width of TiO band are taken into account. Accordingly, the RSG candidates are divided into the early-type (K0-M2) and late-type (after M2) groups during the process.

### 3.1. Preliminary sample of RSGs in the EW(CaT) v.s. $BP - RP$ diagram

#### 3.1.1. EW(CaT) of RSGs

The CaT is a characteristic absorption feature in the near-infrared spectrum, with wavelengths centered at 8498, 8542, and 8662 Å in air (see e.g. Contursi et al. (2021); Creevey et al.

(2023); Fouesneau et al. (2023)). It serves as a strong indicator of luminosity class (i.e., surface gravity), where lower surface gravity typically corresponds to stronger CaT absorption, resulting in a larger EW(CaT). Therefore, using EW(CaT) to identify RSGs is a reasonable approach, and this has been applied in previous studies. Humphreys et al. (1988) classified stars with EW(CaT) greater than 1.1 nm as supergiants when analyzing RSG spectra in M31. Negueruela et al. (2011), focusing only on the 8542 and 8662 Å lines, found that Galactic RSGs earlier than M3 satisfied  $\text{EW}(\text{Ca II } 8542 + \text{Ca II } 8662) > 0.9$  nm. Within the same luminosity class, EW(CaT) increases from F- or G-type stars until it saturates at around M2, after which it rapidly decreases with later spectral type. This decline is due to the increasing prominence of TiO in late-type stars, which erodes both the continuum and atomic lines, thus reducing the equivalent width of CaT.

Although this trend has been proved in previous studies (see Figure 4 in Negueruela et al. (2011) and Figure 9 in Dorda et al. (2016)), 185 known Galactic RSGs are selected to quantitatively examine the variation of EW(CaT) with spectral type. Their EW(CaT) measurements are taken from Cesetti et al. (2013), Dorda et al. (2018), Diczenco & Levesque (2019) or this work with RVS spectra. Figure 4 illustrates the relation between EW(CaT) and spectral type for these stars, displaying the same trend as previously described. Early-type RSGs (up to M2) have  $\text{EW}(\text{CaT}) > 1.1$  nm which is consistent with the definition by Humphreys et al. (1988). In Figure 4, the EW(CaT) value at M6 has a large dispersion, which is because of the difficulties in determining the spectral type of late-M RSGs, as they are variable. For instance, the star with the largest EW(CaT) at M6 is the well-known NML Cyg, whose spectral type is reported to range from M4.5 to M7.9 (Samus' et al. 2017). NML Cyg is a supergiant, potentially even a hypergiant, and its EW(CaT) is expected to be larger than that of stars with similar spectral types. Conversely, the star with the smallest EW(CaT) at M6 is V577 Cep, whose spectral type is reported to range from M6 to M8 (Skiff 2014). Nakamura et al. (2016) included V577 Cep in their catalog of nearby RSG candidates, although they claimed the possibility that their sample may contain red giants with luminosity class of II or III. A linear fitting is applied to build the relation of EW(CaT) with spectral type later than M2, requiring the fitting to pass through the M2 type at  $\text{EW}(\text{CaT}) = 1.1$  nm, as shown by the black line in Figure 4. This provides an approximate EW(CaT) values for RSGs of later spectral types, which is listed in Table 1. It can be noted that the EW(CaT) decreases to 0.230 nm at M8.

#### 3.1.2. $(BP - RP)_0$ of RSGs

The intrinsic color index  $(BP - RP)_0$  is calculated to constrain the minimal observational  $BP - RP$  for specific sub-type which is associated with the EW(CaT). In addition, RSGs are usually more luminous than other type of stars and experience higher interstellar extinction to appear redder. The MIST model (Paxton et al. 2011, 2013, 2015; Dotter 2016; Choi et al. 2016) is used to generate evolutionary tracks for stars with initial mass between 8–40  $M_{\odot}$ , assuming  $v/v_{\text{crit}} = 0.4$ ,  $[\text{Fe}/\text{H}] = 0$ , and  $A_V = 0$ . Subsequently, the temperature scale for Galactic RSGs from Levesque et al. (2005) is adopted to determine the effective temperature ( $T_{\text{eff}}$ ) for each spectral subtype. The  $T_{\text{eff}}$  for K1, M0, M1, M2, M3, M4, and M5 RSGs is set at 4100K, 3790K, 3745K, 3660K, 3605K, 3535K and 3450K respectively, and the values of  $(BP - RP)_0$  are presented in Table 1.

### 3.1.3. The EW(CaT) vs. $BP - RP$ diagram

The EW(CaT) vs.  $BP - RP$  diagram serves as a substitute of the EW(CaT) vs. spectral type diagram (Figure 4) to define the region of RSGs. Because no spectral type information is available for all selected RVS sources, the observational  $BP - RP$  is used as an indicator. The EW(CaT) of the remaining sources are calculated through the method described in Section 2.2.2, and the comparison of EW(CaT) with Dorda et al. (2018) indicates high consistency, as it can be fitted with  $EW(CaT)_{\text{Dorda+18}} = 1.1 \times EW(CaT)_{\text{Thiswork}} - 0.05$  nm with a root-mean-square dispersion of 0.057 nm. The error in equivalent width is calculated by using the equation in Vollmann & Eversberg (2006):

$$\sigma(W_\lambda) = \sqrt{1 + \frac{F_C}{\bar{F}} \cdot \frac{(\Delta\lambda - W_\lambda)}{S/N}} \quad (1)$$

where  $F_C$  represents the continuum flux,  $\bar{F}$  is the average flux over the measured wavelength range,  $\Delta\lambda$  is the wavelength range,  $W_\lambda$  is the equivalent width of the line, and  $S/N$  is the SNR of the spectrum. The absolute error of EW(CaT) is presented as  $\sigma(EW(CaT))$ , and the relative error is then defined as  $\sigma(EW(CaT))/EW(CaT)$ . For example, with  $SNR = 100$  and  $EW(CaT) = 0.5$  nm, a typical  $\sigma(EW(CaT))$  is around 0.07 nm. According to Equation 1,  $\sigma(EW(CaT))$  is expected to be inversely proportional to both the EW(CaT) itself and the SNR. Therefore, smaller equivalent widths and lower SNR will naturally lead to larger measurement errors.

Figure 5 presents the EW(CaT) vs.  $BP - RP$  diagram, where all selected RVS sources are displayed with density-based color coding. In order to clarify the locations of different classes of stars, the sample stars are cross-identified with the APOGEE DR17 (Abdurro'uf et al. 2022) catalog which provide stellar atmospheric parameters from high-resolution near-infrared spectroscopic survey. This results in 6905 and 4295 stars with  $\log g = 2 - 3$  and  $\log g > 3.5$ , which are considered as red giants and dwarfs, respectively. As displayed in the right panel of Figure 5, the area of the dwarfs and red giants are clearly defined, which are two high-density regions with EW(CaT) equal to 0.4-0.7 nm and 0.6-0.9 nm, respectively. Additionally, the branch that decline from 1.5 to 3 in  $BP - RP$  is of M-dwarfs, which is confirmed by their high proper motion measured by Gaia, because they are close to us.

With the results from Section 3.1.1 and 3.1.2, the bluest boundary of the Galactic RSGs is delineated in Figure 5 by the solid red line. The upper lines are determined by the  $(BP - RP)_0 = 1.548$  for K1-type RSGs and an EW(CaT) value of 1.1 nm before M2. For M2 to M5 types, a linear fitting between EW(CaT) and  $(BP - RP)_0$  is used to describe the approximate bluest boundary of RSGs in the EW(CaT) vs.  $BP - RP$  diagram. Since the  $T_{\text{eff}}$  and  $(BP - RP)_0$  for RSGs later than M5 are unknown, a roughly parallel line to the right branch of the RVS sources is manually drawn to indicate the boundary for later-type RSGs. The known Galactic RSGs (as described in Section 3.1.1) indicated by blue dots in Figure 5 are all on the right side of the boundary lines. Moreover, 576 stars with  $\log g < 1$  from the APOGEE catalog, which are considered to be candidates of supergiants, are also located in this area. Further inspection reveals that sources located to the left of the boundary line have lower metallicity, indicating that they are unlikely to be young, metal-rich RSGs. Both results demonstrate that the boundary lines are reasonable.

Following the boundary lines, the RSG candidates are distributed in two areas in Figure 5, which are separated by the red

dashed line at  $EW(CaT) = 1.1$  nm. Stars above and below this line are classified into the early-type and late-type RSG candidates, respectively, because the former have  $EW(CaT) > 1.1$  nm, and the latter have EW(CaT) less than this value. As to the late-type candidates, the EW(CaT) decreases with  $BP - RP$ , suggesting these stars are late-M type bright stars. Although the intrinsic color index of RSGs is almost the same as dwarfs or giants, the observed color index is significantly red because high-luminosity RSGs experience much more extinction. Therefore these objects are on the right branch in Figure 5 as expected.

### 3.2. The early-type RSG candidates

As described in Section 3.1.3, early-type RSG candidates in our sample are defined as sources with  $BP - RP > 1.584$  and  $EW(CaT) > 1.1$  nm. Out of the remaining 105,652 sources, 30 meet these criteria, which are presented in Table 2. The relative errors of EW(CaT) of all 30 stars are below 6%, as their EW(CaT) values are sufficiently large, ensuring precise measurements. Gaia DR3 provides stellar spectral types through the column `spectral_type_esphs` in the `astrophysical_parameters` table, which includes OBAFGKM and C stars. This classification is primarily based on specific spectral features in BP/RP spectra, such as the dominance of CN and  $C_2$  bands in carbon stars, and the presence of TiO and VO in M-type stars (Lebzelter et al. 2023; Messineo 2023). Among the 30 early-type RSG candidates, 24 and 4 are marked as K-type and M-type stars, respectively, which aligns with expectations since these candidates are expected to be late-K or early-M types. One source is marked as a Cstar (source\_id: 5853442496285943424). But its XP spectrum does not show any significant carbon absorption bands when compared with the XP spectra library of C-rich star of Messineo (2023), suggesting this is likely a misclassification by Gaia. Another source is marked as an O-type star (source\_id: 5546711192039738752), but its XP spectrum is not blue-peaked, while with clear TiO absorption features, indicating this is a late-type M star.

Regarding stellar parameters, five stars in the sample have available Apsis GSP-phot parameters, which are derived by fitting XP spectra using PHOENIX or MARCS models to provide best-fit estimates of  $T_{\text{eff}}$ ,  $\log g$ , and  $[Fe/H]$  (Andrae et al. 2023; Fouesneau et al. 2023). Their  $T_{\text{eff}}$  values are 4451K, 4455K, 4524K, 4568K, and 5123K, with  $\log g$  values between 0.87 and 1.58, consistent with early-type RSG characteristics. However, as described in Fouesneau et al. (2023), the `logposterior_gspphot` column indicates the quality of the Apsis GSP-phot fitting, with higher values for better fittings. It is recommended to only use results with `logposterior_gspphot`  $> -1000$ . Unfortunately, the highest value among these five stars is -9000. As Messineo (2023) pointed out, the Gaia Apsis pipeline struggles to handle bright late-type stars due to their significant variability and fitting challenges, suggesting that these parameters may not be highly reliable and should be treated cautiously.

Additionally, 28 stars in the sample have Apsis GSP-spec parameters, which are derived from RVS spectra (Recio-Blanco et al. 2023). Following recommendations from Recio-Blanco et al. (2023) and Messineo (2023), sources are filtered by requiring the first nine digits of `f1ags_gspspec` to be less than or equal to 1, and the 10th to 12th digits to be non-null. Moreover, Recio-Blanco et al. (2023) indicated that due to parameterization issues in GSP-Spec, cool stars with  $T_{\text{eff}} \lesssim 4000$ K had their parameters set to  $T_{\text{eff}} = 4250 \pm 500$ K and  $\log g = 1.5 \pm 1$ . After accounting for these limitations, eight stars remain with reliable

parameters. Their  $T_{\text{eff}}$  ranges from 3782K to 4632K, and  $\log g$  values span from -0.29 to 0.65, which are also consistent with typical RSGs.

In summary, the stellar parameters derived from the Gaia Apsis pipeline coincides with RSGs for the 30 early-type candidates, in spite that they suffer large uncertainty.

### 3.3. The late-type RSG candidates

#### 3.3.1. TiO band

As described in Section 3.1.3, late-type RSGs can only be distributed along the right branch of Figure 5, where  $\text{EW}(\text{CaT}) < 1.1$  nm, and on the right side of the red solid line. This subset contains 20,873 stars. Because late-type RSGs are cool, oxygen-rich stars, their spectra should feature strong TiO bands. Typically, TiO absorption starts to appear in M2-type stars, peaks at M6, and then saturates. Prominent TiO bands in RSGs include those at 8432+8442+8452 Å and 8859 Å, unfortunately, none of these are covered by the RVS spectra. On the other hand, the XP spectra covers a wide wavelength range, including several strong TiO bands, which are used to screen oxygen-rich M-type stars.

Messineo (2023) identified five TiO absorption features in their XP spectral library, centered approximately at 670, 715, 770, 850, and 940 nm. Given that the 940 nm region also includes absorption from ZrO and CN, only the first four bands are used. Specifically, four wavelength ranges are examined, i.e. 654-698 nm, 698-750 nm, 750-818 nm, and 818-880 nm. If a single local minimum is detected within any of these ranges, TiO absorption is considered present, and its equivalent width is measured. The equivalent width is calculated by linearly fitting the endpoints of each range to represent a pseudo-continuum, following the method described in Section 2.2.2. This approach is reasonable because the endpoints for each range are chosen at the flux maxima of true M-type oxygen-rich stars, and the region between two adjacent flux peaks is designated as the TiO absorption band as shown in Figure 6. This also minimizes the potential contamination by C or S-type stars, as their dominant molecular bands and flux minima are located at different wavelengths, producing distinctly different spectral shapes (Lebzelter et al. 2023). It can be seen in Figure 6 that the spectral shape of C star and S-type star is quite different from oxygen-rich star, making the classification reliable. For insurance, only sources that exhibit TiO absorption in at least two of the four bands are considered true M-type oxygen-rich stars. The equivalent widths of all detectable TiO bands are averaged to yield a single  $\text{EW}(\text{TiO})$  value. Consequently, 1,480 stars are excluded from the sample, 848 of which are excluded due to the lack of XP spectra.

Figure 7 shows the distribution of  $\text{EW}(\text{TiO})$  in the right branch of  $\text{EW}(\text{CaT})$  vs.  $BP - RP$  diagram. It reveals that smaller and larger  $\text{EW}(\text{TiO})$  values correspond to bluer and redder sources, respectively. Since TiO is a reliable indicator of spectral type, the descending branch on the right side of Figure 7 corresponds to an increase in spectral type. This is further supported by the relation between  $\text{EW}(\text{TiO})$  and  $T_{\text{eff}}$  from APOGEE measurements, as shown in the left panel of Figure 8. A comparison between  $\text{EW}(\text{TiO})$  and  $\log g$  from APOGEE is also presented in the right panel of Figure 8, which shows that higher  $\text{EW}(\text{TiO})$  values correspond to lower  $\log g$ , and vice versa, consistent with the conclusions of Negueruela et al. (2011) (see their Figure 3). The GSP-phot parameters are used to check the relation because they are available for many more sources, although with relatively large uncertainty. As shown in gray dots in Figure 8, this trend is confirmed.

The remaining 20,873 stars up to present include late-type RGBs, RSGs, and AGB stars. There are two reasons to suggest that the blue dots in Figure 7 likely represent late-type RGB stars, i.e., close to the tip-RGB. First, Dixon et al. (2023) identified metal-poor tip-RGB stars at high Galactic latitudes, with  $BP - RP$  ranging from 1.55 to 2.25. For sources with higher metallicity or lower Galactic latitudes, the color would be redder, which aligns with the stars with  $BP - RP < 3$  (blue dots in Figure 7). Second, these blue points generally exhibit  $\text{EW}(\text{TiO})$  values below 5-10 nm, which correspond to sources with  $\log g > 1$  in Figure 8, a characteristic of bright giants. Additionally, Figure 9 shows a bimodal distribution of  $\text{EW}(\text{TiO})$ , further indicating the presence of two distinct stellar populations. To minimize contamination from late-type red giants, only sources with  $\text{EW}(\text{TiO}) > 10$  nm are selected, leaving 13,316 stars.

#### 3.3.2. VO band

Both TiO and VO are excellent temperature indicators. After TiO, VO only starts to appear in extremely late-type stars, beginning with M6-type (Kirkpatrick et al. 1991; MacConnell et al. 1992). In Section 3.3.1, it is mentioned that the descending branch on the right side of Figure 5 should indicate an increase in spectral type. To further support this point, the only VO band within the RVS spectral range at 8624 Å in air, (Dorda et al. 2016) is measured.

For this VO band, following the analysis of Dorda et al. (2016), its equivalent width is measured within the range 8624.25-8625.5 Å in air, corresponding to 862.66-862.79 nm in vacuum, and the value is denoted as  $\text{EW}(\text{VO})$ . Figure 10 presents the relation between  $\text{EW}(\text{VO})$  and  $\text{EW}(\text{TiO})$ , showing all the sources with TiO absorption (i.e., including the sources excluded in Section 3.3.1 with  $\text{EW}(\text{TiO}) < 10$  nm). The intensity of the TiO band increases with spectral type (i.e., as temperature decreases), which manifests as a vertical branch on the left side of the figure. TiO absorption saturates around M6, at which point VO begins to appear and strengthens, forming a horizontal branch on the right side. It is evident that the horizontal branch corresponds to redder sources indicated by a large  $BP - RP$ , which aligns with the far-right region in Figure 5. This suggests that the latest-type stars are located in this region. However, since the red wing of the diffuse interstellar band (DIB) near 8621 Å may invade the VO band (Zhao et al. 2021; Gaia Collaboration et al. 2023a; Zhao et al. 2024), and this VO band is so weak that it is difficult to measure at low SNR, this analysis is only presented for demonstration and is not used as a selection criterion.

#### 3.3.3. Removal of AGB stars

At this point, the only potential contamination in the sample comes from AGB stars. Given that AGB stars are generally long-period variables (LPV) with more significant mass loss and larger variation amplitudes than RSGs, the diagram of  $K - W3$  vs.  $BP$  amplitude and period-amplitude sequence are used to exclude mass-losing AGB stars and low mass-loss AGB stars, respectively.

The  $K$  and  $W3$  magnitudes are taken from the Two Micron All Sky Survey (2MASS, Skrutskie et al. (2006)) and ALLWISE (Cutri et al. 2021) catalog respectively. The  $BP$  amplitude is defined by Belokurov et al. (2017) as

$$BP \text{ Amplitude} = \sqrt{\text{phot\_bp\_n\_obs}} \times \frac{\text{phot\_bp\_mean\_flux\_error}}{\text{phot\_bp\_mean\_flux}}$$

(2) `spectraltype_esphs` classifications, all 6196 stars are labeled as M-type, which is encouraging since the sample is indeed expected to contain only O-rich M-type stars. Again, due to the limitations in Gaia Apsis pipeline of bright late-type stars (Messineo 2023), nearly all of the  $\sim 1900$  stars with available GSP-phot parameters have `logposterior_gspphot` values below -1000, indicating that their GSP-phot parameters may be unreliable. Nevertheless, the majority of `teff_gspphot` values fall between 3200-3800K ( $\sim 99\%$ ), and `logg_gspphot` values range from -0.4 to 0.9 ( $\sim 99\%$ ), which are consistent with the expected characteristics of RSGs. Among the 72 stars with APOGEE measurements, their  $T_{\text{eff}}$  and  $\log g$  range from 3300-3800K and 0.1-1.2, respectively, further confirming the robustness of the selection criteria.

## 4. Discussion

### 4.1. The known RSGs

Among the 185 known Galactic RSGs mentioned in Section 3.1.1, 14 have RVS spectra with  $\text{SNR} > 100$ , and four of them are identified as late-type RSGs in our analysis. Of the remaining stars, two lack  $W3$ -band photometry, while eight have  $K - W3$  color  $> 0.5$ . In addition, a cross-match with the RSGs identified by Messineo & Brown (2019) yield 23 stars, 15 of which are absent in the 185 known RSGs. Among these 15 stars, one of them lies to the left of the blue boundary in Figure 5, and another has the XP spectra characteristics of S-type stars, both of which Messineo & Brown (2019) classified into the F-region, suggesting they are unlikely to be RSGs. Ten of the remaining stars have  $K - W3 > 0.5$ , leaving three confirmed as late-type RSG candidates in our sample. The RSGs retained and removed in this work are shown in Figure 13 as purple (22) and blue crosses (7), respectively. None of the sources listed in other well-known Galactic RSG catalogs are present in the initial sample of this study, i.e. no RVS spectrum with  $\text{SNR} > 100$  in Gaia DR3.

### 4.2. Completeness and purity

This study identified 30 early-type and 6196 late-type RSG candidates, respectively. Their distribution in the  $\text{EW}(\text{CaT})$  vs.  $BP - RP$  diagram is shown in Figure 13. For early-type RSG candidates, the criteria of  $BP - RP > 1.584$  and  $\text{EW}(\text{CaT}) > 1.1$  nm ensure a sufficiently complete sample from the released RVS spectra, as these are fundamental characteristics of RSGs. However, potential contamination may arise from yellow supergiants, which share similar  $\text{EW}(\text{CaT})$  values and slightly bluer  $BP - RP$ . If subject to significant extinction, these yellow supergiants could fall within our selection. Another influencing factor is the uncertainty in the  $\text{EW}(\text{CaT})$  measurements. Taking into account the 6% relative error described in Section 3.2, under the most stringent conditions, only stars with  $\text{EW}(\text{CaT}) > 1.166$  nm (i.e.,  $1.1 \times 106\%$ ) can be identified as early-type RSG candidates, resulting in 8 such sources. Under the most lenient conditions, an  $\text{EW}(\text{CaT}) > 1.034$  nm would be sufficient to consider a star an RSG candidate, leading to 394 sources.

For late-type RSGs, the requirement of  $\text{EW}(\text{TiO}) > 10$  nm when analyzing the XP spectra excludes a portion of sources near  $BP - RP \sim 2.5$ , as evidenced by the absence of candidates in this region in Figure 13. Known RSGs from previous studies do occupy this region, as shown by the blue dots in the left panel of Figure 5, indicating possible incompleteness in our sample. However, as described in Section 3.3.1, late-type red giants are present in this area, and  $\text{EW}(\text{TiO})$  reflects stellar surface grav-

All the remaining sources are shown in Figure 11 (left panel), together with the Galactic AGB stars identified by Suh (2021) using IRAS data (right panel). Considering the color index  $K - W3$  is a well-known indicator sensitive to dust emission (Xue et al. 2016), and the AGB stars from Suh (2021) mostly have  $K - W3 > 0.5$ , such sources in our sample are identified as AGB stars and removed. This criterion is reinforced by the fact that the excluded sources also exhibit larger amplitudes. This process removed 6533 stars from our sample. It is important to note that  $\sim 1400$  stars in the  $K$  band and  $\sim 100$  stars in the  $W3$  band in the sample have poor photometric quality, with their flags not marked as 'A' in the catalog. Further examination reveals that these sources are the brightest stars in the sample, with nearly all having  $K$ -band magnitude  $< 4.5$  and  $W3$ -band magnitude  $< 0.5$ , respectively. Given that such bright stars are more likely to be RSGs, no restriction is applied to the photometric quality for this subset. Instead, only stars with  $K - W3 > 0.5$  are excluded, as they are more likely to be AGB stars.

Low mass-loss AGB stars can be identified by examining their period-amplitude sequences, for which the LPV catalog in Gaia DR3 (Lebzelter et al. 2023) provides an excellent opportunity. Observations of the LMC have confirmed that LPVs build at least five sequences on the period-luminosity diagram (PLD): A, B, C', C, and D (see e.g., Wood et al. (1999)). Sequences A and B have been further divided into several sub-sequences to characterize small-amplitude red giant variables (Soszyński et al. 2007). The PLD is a powerful tool for tracing the evolution of LPVs, as different sequences are often associated with varying metallicity and mass-loss rates (Riebel et al. 2012). McDonald & Trabucchi (2019) studied the characteristics of mass-loss rates on the period-amplitude sequences, finding that sequences A and B typically consist of AGB stars with small amplitudes and low mass-loss rates (less than  $10^{-9} M_{\odot} \text{ yr}^{-1}$ ). On the other hand, Jiang et al. (2024) demonstrated that RSGs tend to fall on sequences a2 and C in the PLD. Given the well-studied PLD of the LMC, the RSGs in the LMC can be used to mark a reference region on the period-amplitude diagram, with sequences to the left of the region likely corresponding to low mass-loss AGB stars. By cross-matching the remaining sample with the Gaia DR3 LPV catalog (Lebzelter et al. 2023), there are 1,180 stars with available amplitude and period. Their distributions on the period-amplitude diagram are shown as black points in Figure 12. For comparison, 235 LMC RSGs from the Ren et al. (2021b) sample, cross-matched with the Gaia DR3 LPV catalog, are displayed as red dots. As shown in Figure 12, the black dots divide into two branches corresponding to shorter and longer periods, while RSGs generally exhibit periods longer than 100 days. This makes sense because RSGs with pulsation periods shorter than 100 days are rarely detected (Ren et al. 2019; Chatys et al. 2019). RSGs with timescales shorter than 100 days usually exhibit irregular variation (Ren & Jiang 2020; Zhang et al. 2024), making it challenging to detect in Gaia's long-cadence light curves. Consequently, the shorter-period branch in Figure 12 likely consists of low mass-loss AGB stars. Based on the reference region for RSGs, we manually draw the blue line shown in Figure 12, stars to the left of which are excluded from our sample. This process results in a final sample of 6196 late-type Galactic RSG candidates from Gaia RVS spectra, as listed in Table 3.

For these late-type RSG candidates, the  $\sigma(\text{EW}(\text{CaT}))$  of  $\sim 99.4\%$  sources are lower than 0.07 nm, while  $\sim 99.6\%$  sources have  $\sigma(\text{EW}(\text{CaT}))/\text{EW}(\text{CaT})$  below 20%, further demonstrating the reliability of the measurements. In Gaia's

ity, supporting the exclusion of stars with  $EW(\text{TiO}) < 10$  nm to avoid contamination from red giants. This decision reflects a balance between pureness and completeness, where pureness takes priority.

In addition, the use of the  $K - W3 < 0.5$  criterion likely results in the exclusion of some high-luminosity RSGs, which also possess abundant circumstellar dust caused by significant mass loss. This is indicated by the lack of sources in the lower right corner of Figure 13, where such RSGs are expected to reside. The clustering of blue crosses at the red end in Figure 13 confirms this again, as they are likely late-type high-luminosity RSGs. No constraints on photometric quality are used because sources with poorer photometric quality tend to be brighter, making them more likely to be RSGs. This decision is taken to enhance the completeness of our sample, while it may bring about some AGB stars to contamination. By incorporating additional diagnostics from the mid-infrared or far-infrared, it may be possible to improve the sample's pureness further. Again, this also ensures a pure and relatively complete sample of late-type RSG candidates.

### 4.3. Application to a larger sample

By slightly lowering the SNR threshold to  $SNR > 50$ , the total number of available RVS spectra increases to  $\sim 330,000$ . Applying the process described in Section 3 to these spectra results in the identification of 48 early-type and 11,491 late-type RSG candidates. Although the initial sample size has tripled, the final number of RSG candidates has only doubled. This is expected, as the SNR is correlated with apparent magnitude, meaning that lower SNR sources are likely fainter or of lower photometric quality. It is worth noting that the released RVS spectra do not provide uniform coverage across the sky (Gaia Collaboration et al. 2023b), with noticeably fewer observations in the Galactic plane. Consequently, many RSGs are missed in our sample. We anticipate that the release of the complete RVS spectra in Gaia DR4 will provide a much more comprehensive perspective for identifying RSGs in the Milky Way.

## 5. Summary

RSGs play a crucial role in processes such as interstellar dust production and massive star evolution, making their identification vitally important. While samples of RSGs in nearby galaxies have been expanding greatly thanks to more precise observational data and more effective methods for excluding foreground sources, the search for RSGs within the Milky Way has been slower. This is partly due to the challenges in applying efficient photometric methods, which are hindered by the difficulties in accurately measuring extinction and distance within our galaxy. Moreover, spectroscopic observations have been too inefficient to yield large samples of RSGs. The release of approximately one million RVS spectra in Gaia DR3 offers new possibilities for the search for Galactic RSGs from spectral features.

In this study, high signal-to-noise ratio (SNR greater than 100) RVS spectra are selected as the initial sample. Firstly, the early-type stars are excluded by using the hydrogen Paschen 14 line. Then, by combining the intrinsic color  $BP - RP$  of RSGs across different spectral types with the  $EW(\text{CaT})$ , the bluest boundary of Galactic RSGs on the  $EW(\text{CaT})$  versus  $BP - RP$  diagram can be defined. This allows for the selection of early-type RSGs with  $BP - RP > 1.584$  and  $EW(\text{CaT}) > 1.1$  nm, while removing dwarf stars and the majority of giants, leaving only late-type stars. The analysis of four TiO bands in the XP

spectra helps to identify true O-rich M-type stars, thereby avoiding contamination from C-rich and S-type stars. The equivalent widths of the measured TiO bands are averaged and denoted as  $EW(\text{TiO})$ . Sources with  $EW(\text{TiO}) < 10$  nm are considered late-type red giant branch stars, based on their higher  $\log g$  and bluer colors. The remaining sources are primarily contaminated by AGB stars, where those with mass-loss and those with low mass-loss are identified by  $K - W3 > 0.5$  and period-amplitude sequences, respectively, and are excluded. This process yields a final sample of 30 early-type RSG candidates and 6196 late-type RSG candidates.

Applying this method to the RVS spectra with  $SNR > 50$  results in the identification of 48 early-type RSG candidates and 11,491 late-type RSG candidates. However, due to the uncertainties involved in processing low-SNR spectra, these numbers suffer larger uncertainty. This work serves as a preliminary study in anticipation of Gaia DR4, where the release of a larger volume of spectra is expected to have profound implications for the study of Galactic RSGs.

*Acknowledgements.* We would like to thank the anonymous referee for the constructive suggestions that definitely improved this work. We thank Dr. R. Dorda for providing the line measurements of stars in the Perseus arm (Dorda et al. 2018). This work is supported by the National Natural Science Foundation of China (NSFC) through grants Nos. 12133002, 12203025, and 12373048. National Key R&D Program of China No. 2019YFA0405503, CMS-CSST-2021-A09 and Shandong Provincial Natural Science Foundation through project ZR2022QA064. H.Z. acknowledges the support of the National Natural Science Foundation of China (grant No. 12203099) and the Jiangsu Funding Program for Excellent Postdoctoral Talent. This work has also made use of data from the surveys by Gaia, APOGEE, 2MASS and WISE.

## References

- Abdurro'uf, Accetta, K., Aerts, C., et al. 2022, *ApJS*, 259, 35  
 Alexander, M. J., Kobulnicky, H. A., Clemens, D. P., et al. 2009, *AJ*, 137, 4824  
 Andrae, R., Fouesneau, M., Sordo, R., et al. 2023, *A&A*, 674, A27  
 Astropy-Specutils Development Team. 2019, *Specutils: Spectroscopic analysis and reduction*. Astrophysics Source Code Library, record ascl:1902.012  
 Beasar, E. R., Davies, B., Smith, N., et al. 2020, *MNRAS*, 492, 5994  
 Belokurov, V., Erkal, D., Deason, A. J., et al. 2017, *MNRAS*, 466, 4711  
 Carquillat, M. J., Jäschek, C., Jäschek, M., & Ginestet, N. 1997, *A&AS*, 123, 5  
 Cenarro, A. J., Cardiel, N., Gorgas, J., et al. 2001a, *MNRAS*, 326, 959  
 Cenarro, A. J., Gorgas, J., Cardiel, N., et al. 2001b, *MNRAS*, 326, 981  
 Cesetti, M., Pizzella, A., Ivanov, V. D., et al. 2013, *A&A*, 549, A129  
 Chatys, F. W., Bedding, T. R., Murphy, S. J., et al. 2019, *MNRAS*, 487, 4832  
 Chiavassa, A., Pasquato, E., Jorissen, A., et al. 2011, *A&A*, 528, A120  
 Choi, J., Dotter, A., Conroy, C., et al. 2016, *ApJ*, 823, 102  
 Clark, J. S., Negueruela, I., Davies, B., et al. 2009, *A&A*, 498, 109  
 Contursi, G., de Laverny, P., Recio-Blanco, A., & Palicio, P. A. 2021, *A&A*, 654, A130  
 Creevey, O. L., Sordo, R., Pailler, F., et al. 2023, *A&A*, 674, A26  
 Cropper, M., Katz, D., Sartoretti, P., et al. 2018, *A&A*, 616, A5  
 Cutri, R. M., Wright, E. L., Conroy, T., et al. 2021, *VizieR Online Data Catalog: AllWISE Data Release (Cutri+ 2013)*, *VizieR On-line Data Catalog: II/328*. Originally published in: IPAC/Caltech (2013)  
 Davies, B., Figer, D. F., Kudritzki, R.-P., et al. 2007, *ApJ*, 671, 781  
 Davies, B., Figer, D. F., Law, C. J., et al. 2008, *ApJ*, 676, 1016  
 Decin, L., Richards, A. M. S., Marchant, P., & Sana, H. 2024, *A&A*, 681, A17  
 Diaz, A. I., Terlevich, E., & Terlevich, R. 1989, *MNRAS*, 239, 325  
 Diconzo, B. & Levesque, E. M. 2019, *AJ*, 157, 167  
 Dixon, M., Mould, J., Flynn, C., et al. 2023, *MNRAS*, 523, 2283  
 Dorda, R., González-Fernández, C., & Negueruela, I. 2016, *A&A*, 595, A105  
 Dorda, R., Negueruela, I., & González-Fernández, C. 2018, *MNRAS*, 475, 2003  
 Dotter, A. 2016, *ApJS*, 222, 8  
 Figer, D. F., MacKenty, J. W., Robberto, M., et al. 2006, *ApJ*, 643, 1166  
 Fouesneau, M., Frémat, Y., Andrae, R., et al. 2023, *A&A*, 674, A28  
 Gaia Collaboration, Prusti, T., de Bruijne, J. H. J., et al. 2016, *A&A*, 595, A1  
 Gaia Collaboration, Schultheis, M., Zhao, H., et al. 2023a, *A&A*, 674, A40  
 Gaia Collaboration, Vallenari, A., Brown, A. G. A., et al. 2023b, *A&A*, 674, A1  
 Garmany, C. D. & Stencel, R. E. 1992, *A&AS*, 94, 211  
 Gehrz, R. 1989, in *IAU Symposium, Vol. 135, Interstellar Dust*, ed. L. J. Allamandola & A. G. G. M. Tielens, 445

- Ginestet, N., Carquillat, J. M., Jaschek, M., & Jaschek, C. 1994, A&AS, 108, 359
- Healy, S., Horiuchi, S., Colomer Molla, M., et al. 2024, MNRAS, 529, 3630
- Humphreys, R. M. 1978, ApJS, 38, 309
- Humphreys, R. M. & Davidson, K. 1979, ApJ, 232, 409
- Humphreys, R. M., Helmel, G., Jones, T. J., & Gordon, M. S. 2020, AJ, 160, 145
- Humphreys, R. M., Pennington, R. L., Jones, T. J., & Ghigo, F. D. 1988, AJ, 96, 1884
- Jennings, J. & Levesque, E. M. 2016, ApJ, 821, 131
- Jiang, B., Ren, Y., & Yang, M. 2024, in IAU Symposium, Vol. 376, IAU Symposium, ed. R. de Grijs, P. A. Whitelock, & M. Catelan, 292–305
- Katz, D., Sartoretti, P., Guerrier, A., et al. 2023, A&A, 674, A5
- Kirkpatrick, J. D., Henry, T. J., & McCarthy, Donald W., J. 1991, ApJS, 77, 417
- Kiss, L. L., Szabó, G. M., & Bedding, T. R. 2006, MNRAS, 372, 1721
- Lebzelter, T., Mowlavi, N., Lecoeur-Taibi, I., et al. 2023, A&A, 674, A15
- Levesque, E. M. & Massey, P. 2012, AJ, 144, 2
- Levesque, E. M., Massey, P., Olsen, K. A. G., et al. 2005, ApJ, 628, 973
- MacConnell, D. J., Wing, R. F., & Costa, E. 1992, AJ, 104, 821
- Mallik, S. V. 1994, A&AS, 103, 279
- Mallik, S. V. 1997, A&AS, 124, 359
- Massey, P. 1998, ApJ, 501, 153
- Massey, P. & Olsen, K. A. G. 2003, AJ, 126, 2867
- McDonald, I. & Trabucchi, M. 2019, MNRAS, 484, 4678
- Messineo, M. 2023, A&A, 671, A148
- Messineo, M. & Brown, A. G. A. 2019, AJ, 158, 20
- Nakamura, K., Horiuchi, S., Tanaka, M., et al. 2016, MNRAS, 461, 3296
- Negueruela, I., González-Fernández, C., Marco, A., & Clark, J. S. 2011, A&A, 528, A59
- Negueruela, I., González-Fernández, C., Marco, A., Clark, J. S., & Martínez-Núñez, S. 2010, A&A, 513, A74
- Negueruela, I., Marco, A., González-Fernández, C., et al. 2012, A&A, 547, A15
- Paxton, B., Bildsten, L., Dotter, A., et al. 2011, ApJS, 192, 3
- Paxton, B., Cantiello, M., Arras, P., et al. 2013, ApJS, 208, 4
- Paxton, B., Marchant, P., Schwab, J., et al. 2015, ApJS, 220, 15
- Recio-Blanco, A., de Laverny, P., Palicio, P. A., et al. 2023, A&A, 674, A29
- Ren, Y., Jiang, B., Yang, M., et al. 2021a, ApJ, 907, 18
- Ren, Y., Jiang, B., Yang, M., Wang, T., & Ren, T. 2021b, ApJ, 923, 232
- Ren, Y. & Jiang, B.-W. 2020, ApJ, 898, 24
- Ren, Y., Jiang, B.-W., Yang, M., & Gao, J. 2019, ApJS, 241, 35
- Riebel, D., Srinivasan, S., Sargent, B., & Meixner, M. 2012, ApJ, 753, 71
- Samus', N. N., Kazarovets, E. V., Durlevich, O. V., Kireeva, N. N., & Pastukhova, E. N. 2017, Astronomy Reports, 61, 80
- Sartoretti, P., Katz, D., Cropper, M., et al. 2018, A&A, 616, A6
- Sartoretti, P., Marchal, O., Babusiaux, C., et al. 2023, A&A, 674, A6
- Schödel, R., Najarro, F., Muzic, K., & Eckart, A. 2010, A&A, 511, A18
- Skiff, B. A. 2014, VizieR Online Data Catalog: Catalogue of Stellar Spectral Classifications (Skiff, 2009- ), VizieR On-line Data Catalog: B/mk. Originally published in: Lowell Observatory (October 2014)
- Skrutskie, M. F., Cutri, R. M., Stiening, R., et al. 2006, AJ, 131, 1163
- Soszyński, I., Dziembowski, W. A., Udalski, A., et al. 2007, Acta Astron., 57, 201
- Suh, K.-W. 2021, ApJS, 256, 43
- Vollmann, K. & Eversberg, T. 2006, Astronomische Nachrichten, 327, 862
- Wang, T., Jiang, B., Ren, Y., Yang, M., & Li, J. 2021, ApJ, 912, 112
- Wen, J., Gao, J., Yang, M., et al. 2024, AJ, 167, 51
- Wood, P. R., Alcock, C., Allsman, R. A., et al. 1999, in IAU Symposium, Vol. 191, Asymptotic Giant Branch Stars, ed. T. Le Bertre, A. Lebre, & C. Waelkens, 151
- Xue, M., Jiang, B. W., Gao, J., et al. 2016, ApJS, 224, 23
- Yang, M., Bonanos, A. Z., Jiang, B., et al. 2023, A&A, 676, A84
- Yang, M., Bonanos, A. Z., Jiang, B.-W., et al. 2019, A&A, 629, A91
- Yang, M. & Jiang, B. W. 2012, ApJ, 754, 35
- Zhang, Z., Ren, Y., Jiang, B., Soszyński, I., & Jayasinghe, T. 2024, ApJ, 969, 81
- Zhao, H., Schultheis, M., Qu, C., & Zwitter, T. 2024, A&A, 683, A199
- Zhao, H., Schultheis, M., Recio-Blanco, A., et al. 2021, A&A, 645, A14



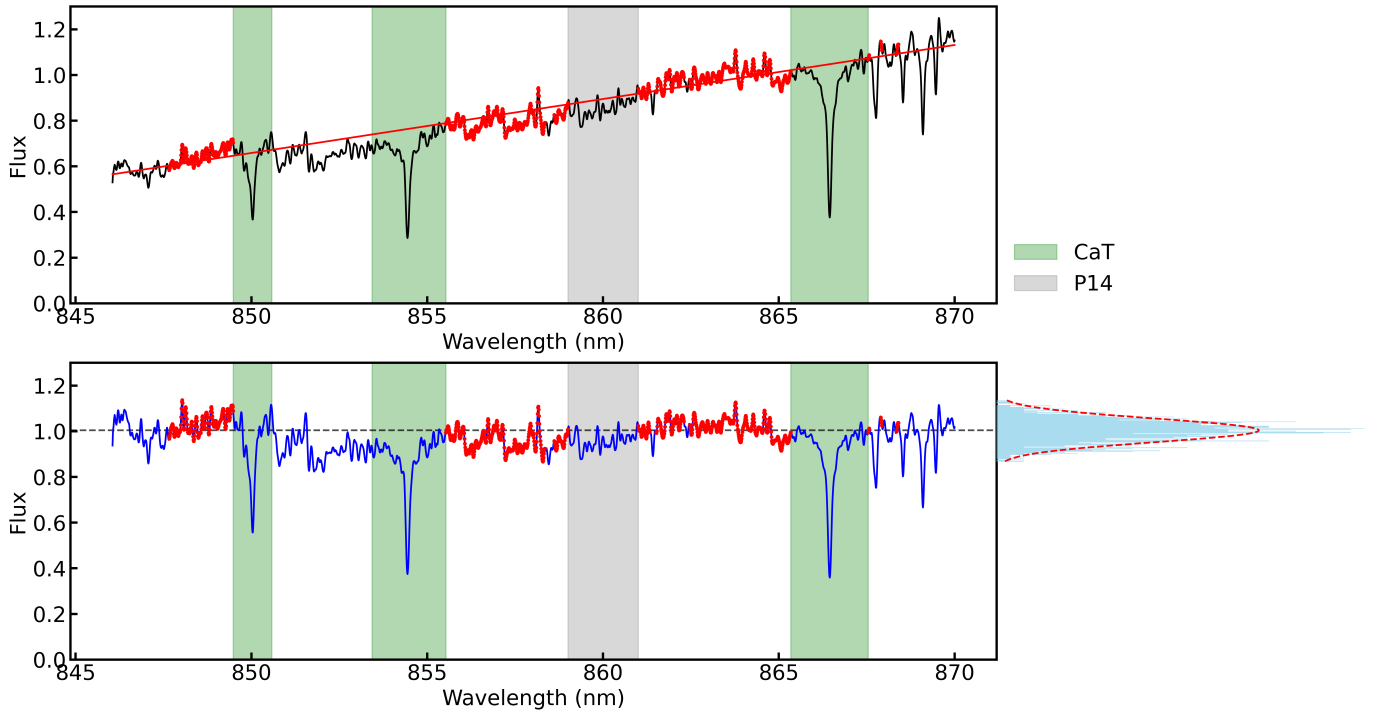


**Fig. 1.** Example of RVS spectrum re-normalization (source\_id: 5836392511305856128). The upper panel shows the original spectrum, and the solid red line is obtained by linear fitting of the red dots. The blue on the bottom panel is the re-normalized spectrum, the histogram on the lower right is a distribution of red dots, and the black dashed line marks the mean of its Gaussian fitting, representing the continuum after re-normalization. The shaded colors are used to represent different absorption lines.

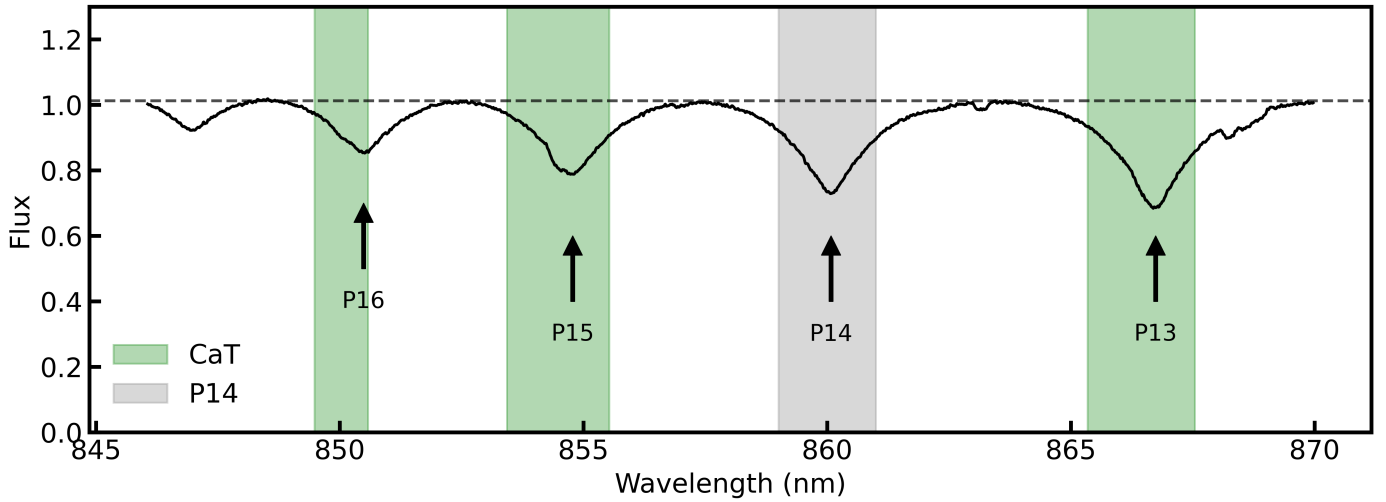


**Fig. 2.** Example of the RVS spectrum of a typical early-type star (source\_id: 2270570062017774976). The position indicated by the arrow marks the Paschen line series P13-P16 for hydrogen. The gray and green shade mark the measuring ranges of P14 and CaT, respectively.

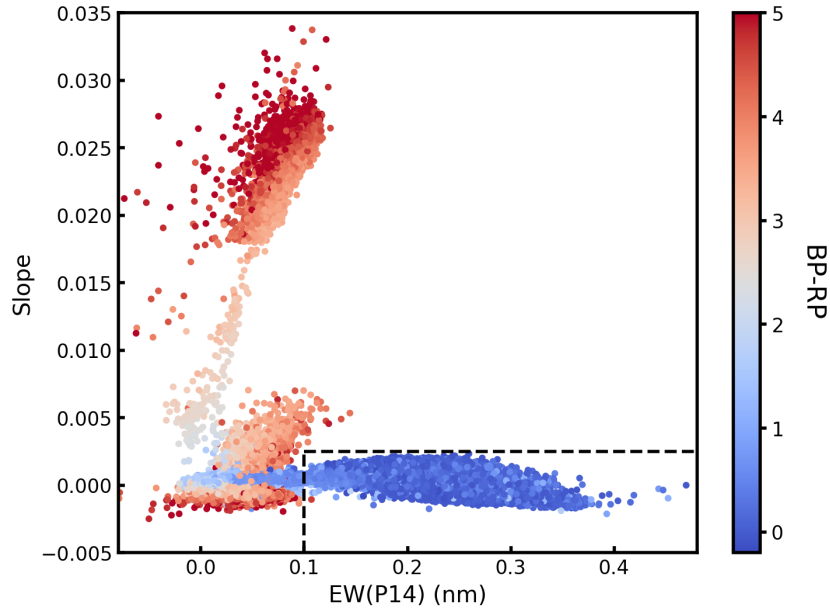


**Fig. 3.** The diagram used to remove early-type stars. The horizontal and vertical axes are EW(P14) and the slope mentioned in Section 2.1, respectively. The black dashed box defines the area of early-type stars, and the dots are color-coded by  $BP - RP$ .

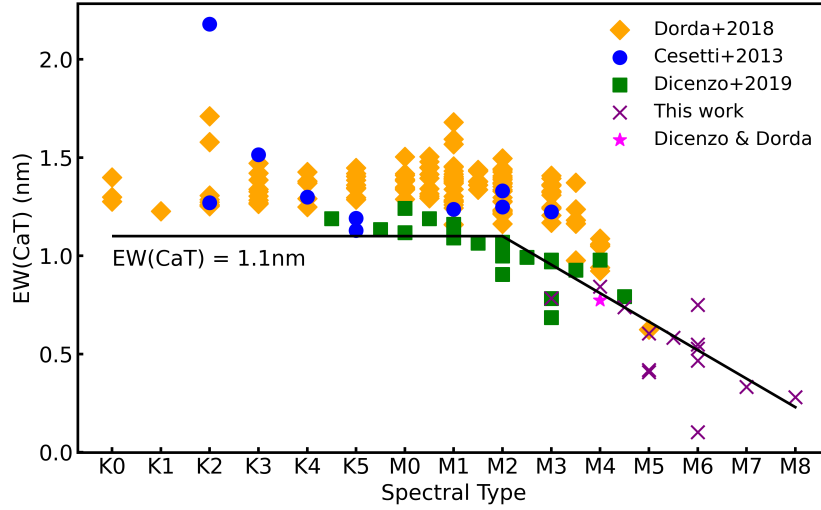


**Fig. 4.** Spectral types versus EW(CaT) for 185 known Galactic RSGs, with their EW(CaT) measurements from [Cesetti et al. \(2013\)](#), [Dorda et al. \(2018\)](#), [Dicenzo & Levesque \(2019\)](#). For the only magenta asterisk, the results of [Dorda et al. \(2018\)](#) and [Dicenzo & Levesque \(2019\)](#) are represented after being averaged. The crosses denote the sources measured in this work from the Gaia RVS spectra. The solid black lines mark  $EW(CaT) = 1.1$  nm (for K-type or early M-type RSGs) and the decreasing of EW(CaT) with spectral type (for RSGs later than M2), respectively.

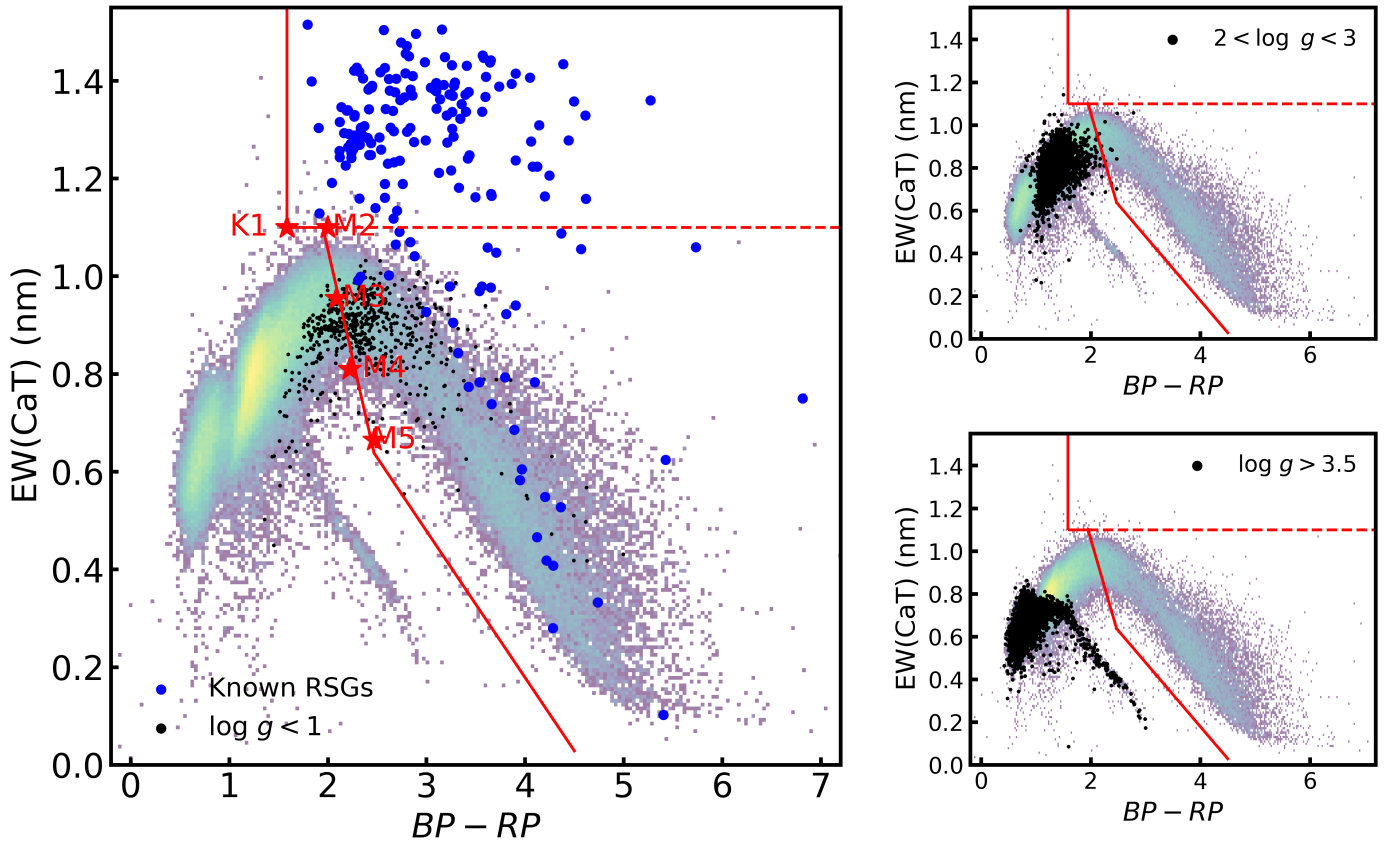


**Fig. 5.** The diagram of  $EW(\text{CaT})$  vs.  $BP - RP$  with color coded by density for all selected RVS objects. Overlaid black dots are those with APOGEE measurements of  $\log g$ . They are plotted separately to represent the positions of different types of stars. The blue dots on the left panel are known Galactic RSGs mentioned in Section 3.1.1. The red asterisks mark the positions of zero-extinction K1 and M2-M5 RSGs. The red solid lines represent the bluest boundary of Galactic RSGs in this diagram, while the red dashed line marks the dividing line between the early and late type RSGs.

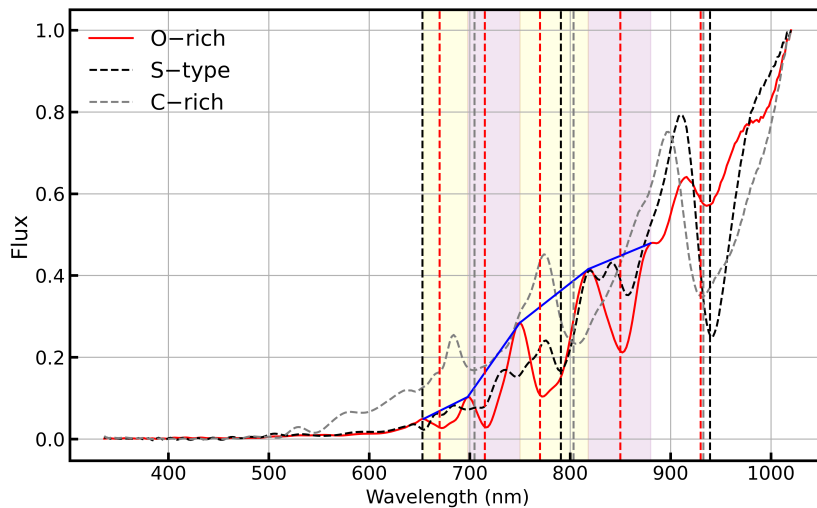


**Fig. 6.** Examples of three XP spectra of an oxygen-rich star (source\_id: 5853243278519978112, red solid line), a carbon-rich star (source\_id: 5716487091710504064, gray dashed line), and an S-type star (source\_id: 5233074194539855360, black dashed line). The spectra are normalized to the maximum flux for comparison. The shaded color is the ranges of the four TiO that is measured. The four blue solid lines represent the pseudo-continuum of measuring equivalent width.

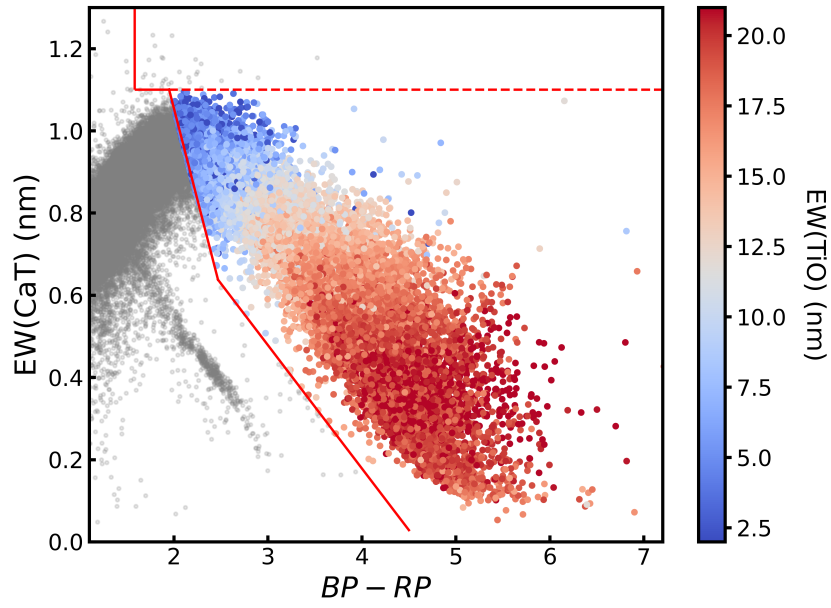


**Fig. 7.** The same as Figure 5, but the regions for late-type RSG candidates are color-coded with  $EW(\text{TiO})$ , and the rest are shown by gray dots.

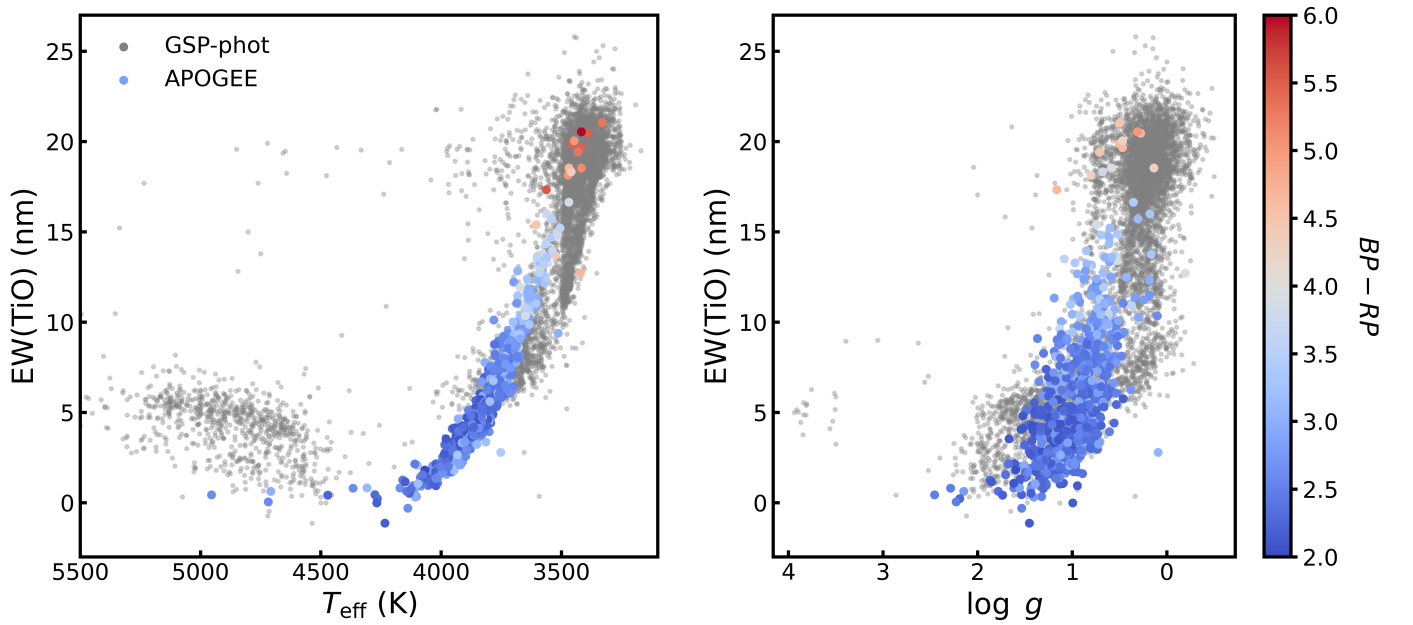


**Fig. 8.** The relation of  $EW(\text{TiO})$  with  $T_{\text{eff}}$  and  $\log g$ . The dots color-coded by  $BP - RP$  are APOGEE measurements, while the gray dots are from Gaia GSP-phot parameters. There are 655 and 5934 stars have available APOGEE and GSP-phot parameters, respectively.

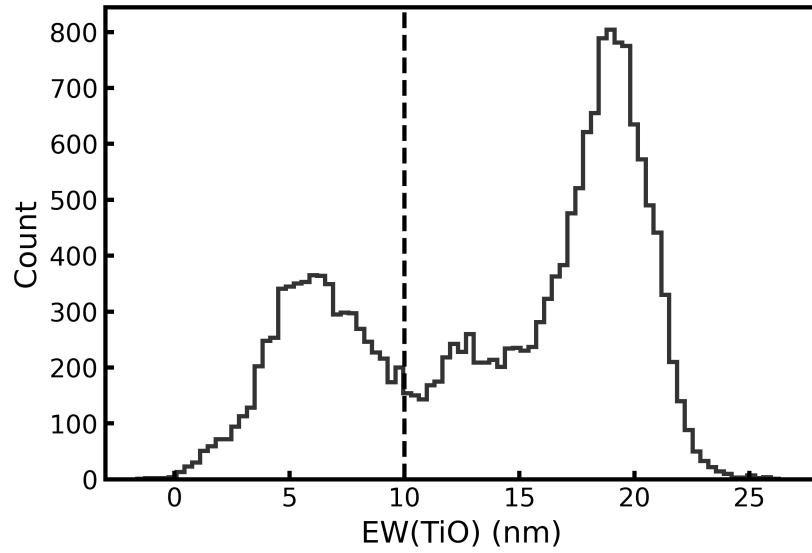


**Fig. 9.** The histogram of EW(TiO). The black vertical line marks the position where EW(TiO) = 10 nm.

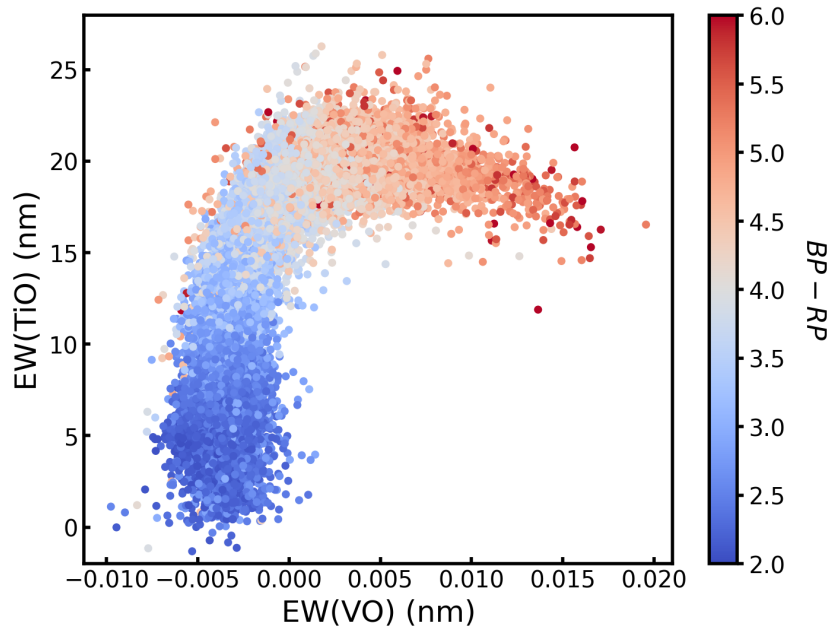


**Fig. 10.** The EW(TiO) vs. EW(VO) diagram for all sources exhibiting TiO absorption. The dots are color coded by  $BP - RP$ .

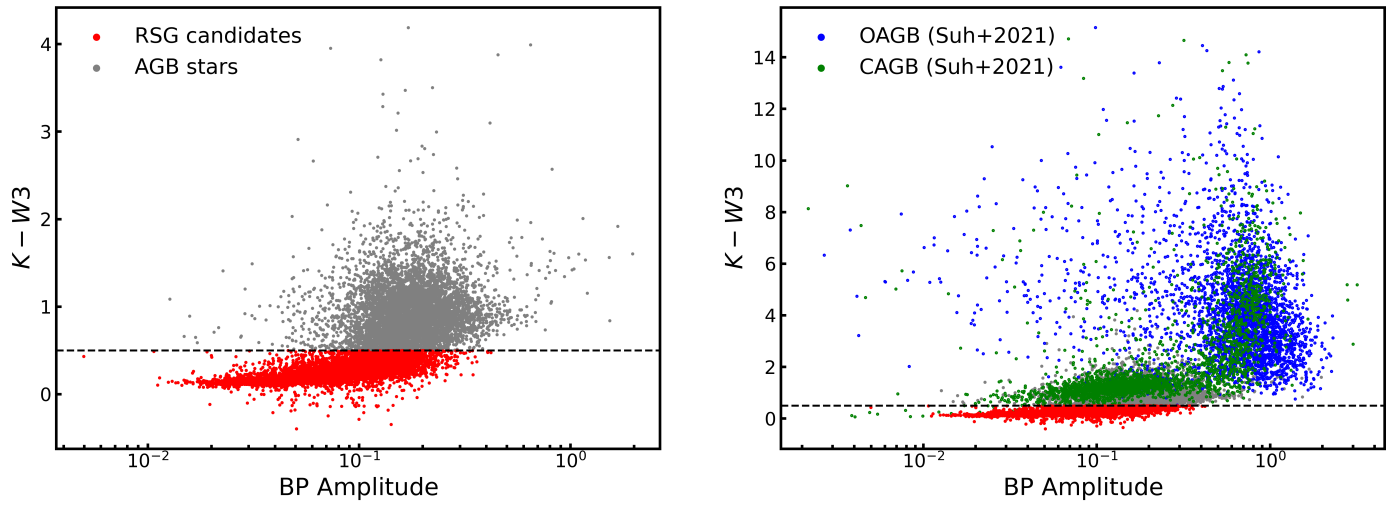


**Fig. 11.** The  $K - W3$  vs.  $BP$  amplitude diagram for stars that have  $EW(\text{TiO}) > 10$  nm. The  $BP$  amplitude is defined by Equation 2. The red dots in both panels are selected late-type RSG candidates, while the gray dots are stars that are considered to be AGB stars. The blue and green dots in the right panel are OAGB and CAGB identified by [Suh \(2021\)](#), respectively.

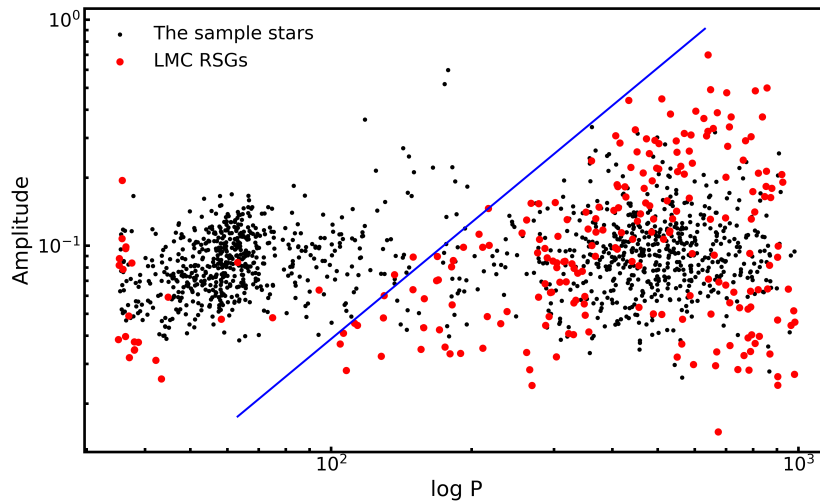


**Fig. 12.** The period-amplitude diagram of our sample stars (black dots) and the LMC RSGs from [Ren et al. \(2021b\)](#) (red dots). The amplitude and period are taken from Gaia DR3 LPV catalog ([Lebzelter et al. 2023](#)). The blue solid line are manually drawn to separate the AGB stars branch (short period) and the RSGs candidate branch (long period).

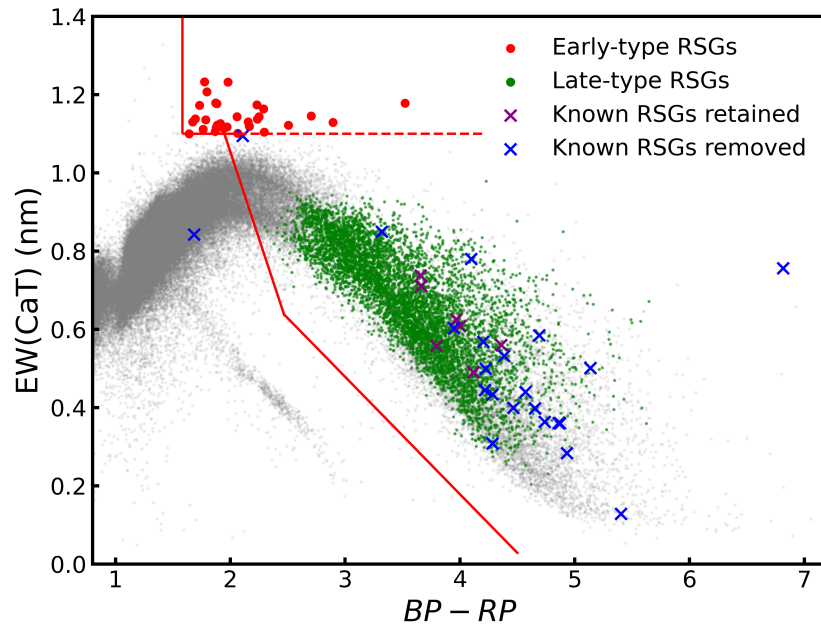


**Fig. 13.** The distribution of RSG candidates selected in this work in the EW(CaT) vs.  $BP - RP$  diagram. The red and green dots are the early-type and late-type candidates, respectively. The purple and blue crosses are known RSGs that retained and removed in this work, respectively.

**Table 1.** The intrinsic color index  $(BP - RP)_0$  of Galactic RSGs and their EW(CaT)

Spectral type	$T_{\text{eff}}$ (K)	EW(CaT) (nm)	$(BP - RP)_0^{\text{MIST}}$
K1	4100	$\geq 1.100$	1.548
M2	3660	1.100	1.999
M3	3605	0.955	2.086
M4	3535	0.810	2.221
M5	3450	0.665	2.469
M6	–	0.520	–
M7	–	0.375	–
M8	–	0.230	–



Table 2. The 30 early-type RSG candidates from Gaia RVS spectra

Gaia ID	R.A. (J2016)	Decl. (J2016)	<i>G</i> (mag)	<i>BP</i> (mag)	<i>RP</i> (mag)	SNR <sup>a</sup>	EW(Ca II 8498) (nm)	EW(Ca II 8542) (nm)	EW(Ca II 8662) (nm)
Gaia DR3 5853442496285943424	217.86998	-62.854653	12.07897	14.265091	10.742440	128.383770	0.235±0.010	0.540±0.019	0.403±0.021
Gaia DR3 5820436432841319296	236.608956	-68.636116	8.634509	9.516343	7.720005	313.891540	0.229±0.004	0.541±0.008	0.437±0.008
Gaia DR3 5820502850214136832	238.263848	-68.346030	11.269479	12.143257	10.358867	102.666626	0.213±0.013	0.519±0.023	0.403±0.026
Gaia DR3 4103709932814452608	278.951953	-14.427099	8.090821	9.066613	7.124403	396.023250	0.209±0.003	0.497±0.006	0.408±0.007
Gaia DR3 5984880628866213760	241.238836	-47.051229	8.543653	9.319298	7.679147	295.434970	0.213±0.004	0.494±0.008	0.394±0.009
Gaia DR3 4093865043071455744	272.231815	-21.402472	7.354873	8.524316	6.293784	583.243000	0.222±0.002	0.530±0.004	0.422±0.005
Gaia DR3 5239689818579893632	160.344604	-65.101892	9.030067	10.026202	8.054391	182.615830	0.210±0.007	0.508±0.013	0.399±0.015
Gaia DR3 4067892929213072512	265.895181	-25.549597	10.125677	11.799958	8.905755	169.187670	0.214±0.008	0.513±0.014	0.402±0.016
Gaia DR3 6073909597165776640	193.698323	-54.162952	11.149422	12.276551	10.111722	128.280530	0.215±0.010	0.514±0.019	0.390±0.021
Gaia DR3 5337904416304099200	165.763401	-61.519718	10.441664	11.438498	9.459789	119.273990	0.237±0.011	0.551±0.020	0.444±0.022
Gaia DR3 5853509983176878592	217.053019	-62.649578	10.917154	12.289372	9.783605	201.837100	0.216±0.007	0.511±0.012	0.395±0.013
Gaia DR3 5853511220127551744	217.048239	-62.579237	11.007373	12.223262	9.928592	122.616776	0.213±0.011	0.498±0.020	0.393±0.022
Gaia DR3 5233812168691960192	178.595879	-70.002198	8.382010	9.311263	7.439888	443.421300	0.226±0.003	0.526±0.005	0.427±0.006
Gaia DR3 5235601284598319616	178.660747	-68.178623	10.442018	11.313028	9.537476	104.256640	0.229±0.013	0.556±0.023	0.447±0.025
Gaia DR3 4102947146590069760	279.198009	-15.945464	6.157430	7.278494	5.123030	527.787800	0.215±0.003	0.510±0.005	0.405±0.005
Gaia DR3 4121402517949300480	263.468978	-20.152666	8.579352	9.793996	7.504721	451.467830	0.223±0.003	0.520±0.005	0.421±0.006
Gaia DR3 4042693875003175808	272.360644	-33.234316	6.880441	7.680243	6.007875	489.989320	0.211±0.003	0.509±0.005	0.411±0.005
Gaia DR3 5636119113908970752	137.732247	-28.473395	9.551785	10.490046	8.603405	296.026820	0.209±0.005	0.511±0.008	0.403±0.009
Gaia DR3 5267828417053112576	110.118788	-69.769439	10.266059	11.085389	9.391768	135.958080	0.213±0.010	0.522±0.018	0.403±0.020
Gaia DR3 867070063597368064	115.243793	23.018474	5.330736	6.187736	4.425474	441.684400	0.208±0.003	0.506±0.005	0.397±0.006
Gaia DR3 5606087946667386624	108.496223	-30.004131	10.214938	11.056752	9.324802	165.470350	0.219±0.008	0.529±0.015	0.424±0.016
Gaia DR3 4068970240056037504	267.321884	-22.491656	10.703414	11.622157	9.754555	122.038020	0.215±0.011	0.494±0.020	0.397±0.022
Gaia DR3 5845475886035405312	198.814510	-67.919802	10.728763	11.665064	9.783031	110.186510	0.223±0.012	0.528±0.022	0.426±0.024
Gaia DR3 4058702248983652096	262.457118	-29.780555	9.034603	9.963396	8.086934	150.555650	0.216±0.009	0.499±0.016	0.401±0.018
Gaia DR3 5514740550687176960	124.620115	-50.481626	9.321692	10.272155	8.359034	235.037890	0.216±0.006	0.504±0.010	0.406±0.011
Gaia DR3 6004968534471349376	226.521595	-40.550913	10.425404	11.590588	9.354713	105.546530	0.188±0.013	0.522±0.023	0.427±0.025
Gaia DR3 6723841434427244416	278.550854	-39.303318	9.025936	10.073758	8.016438	273.550870	0.214±0.005	0.517±0.009	0.413±0.010
Gaia DR3 5515454717849642624	127.087196	-48.134389	10.079885	11.600745	8.895877	171.946580	0.218±0.008	0.519±0.014	0.408±0.016
Gaia DR3 3155188292539070208	109.034100	8.823780	9.506177	10.560427	8.496337	131.214870	0.206±0.010	0.500±0.019	0.395±0.020
Gaia DR3 5546711192039738752	123.739687	-33.449050	8.767647	9.926933	7.676443	384.052580	0.217±0.003	0.509±0.006	0.418±0.007

**Table 3.** The 6196 late-type RSG candidates from Gaia RV/S spectra

Gaia ID	R.A. (J2016)	Decl. (J2016)	G (mag)	BP (mag)	RP (mag)	SNR	EW(Ca II 8498) (nm)	EW(Ca II 8542) (nm)	EW(Ca II 8662) (nm)	K (mag)	W3 (mag)	EW(TiO) (nm)
Gaia DR3 5912905292012078080	263.831986	-58.796211	10.944374	13.220857	9.563824	164.047710	0.062±0.009	0.252±0.016	0.209±0.018	5.899	5.480	17.653
Gaia DR3 5912586227479692800	262.643347	-59.522606	10.615781	13.111814	9.200260	155.498920	0.045±0.010	0.234±0.017	0.169±0.019	5.439	5.209	20.464
Gaia DR3 2269271710582159232	277.967082	75.698835	9.047530	10.693685	7.799423	244.999390	0.152±0.006	0.392±0.010	0.327±0.011	4.730	4.580	12.248
Gaia DR3 2265488703388096896	283.316176	70.711737	10.098157	11.943086	8.815959	217.533920	0.124±0.007	0.343±0.012	0.294±0.013	5.608	5.431	15.031
Gaia DR3 5902334724683114880	227.324252	-49.648354	11.454111	14.084639	10.028410	101.382140	0.071±0.015	0.262±0.027	0.202±0.029	5.998	5.782	19.736
Gaia DR3 59024177034445930624	228.320978	-49.174342	10.891149	13.215270	9.530221	120.433140	0.105±0.012	0.306±0.022	0.260±0.024	5.820	5.557	16.115

**Notes.** (This table is available in its entirety in machine-readable form.)